High performance of carbon nanotube elastocaloric refrigerators over a large temperature span

Tatiana Naomi Yamamoto Silva and Alexandre F. Fonseca*

Applied Physics Department, Institute of Physics "Gleb Wataghin," University of Campinas - UNICAMP, 13083-859 Campinas, São Paulo, Brazil

(Received 23 June 2022; revised 2 September 2022; accepted 29 September 2022; published 13 October 2022)

Compression of greenhouse gases still dominates the market of refrigeration devices. Although well established and efficient, this technology is neither safe for the environment nor able to be scaled down to nanoscale. Solid-state cooling technologies are being developed to overcome these limitations, including studies at nanoscale. Among them, the so-called elastocaloric effect (eC) consists of the thermal response ΔT of a material under strain deformation. In this work, fully atomistic molecular dynamics simulations of the eC in carbon nanotubes (CNTs) are presented over a large temperature span. The efficiency of the CNTs as solid refrigerators is investigated by simulating their eC in a model of refrigerator machine running under Otto-like thermodynamic cycles (two adiabatic expansion/contraction plus two isostrain heat exchange processes) operating at temperatures T_O ranging 300–2000 K. The coefficient of performance (COP), defined as the ratio of heat removed from the cold region to the total work performed by the system per thermodynamic cycle, is calculated for each value of T_O. Our results show a nonlinear dependence of ΔT on T_O, reaching a minimum value of about 30 K for T_O between 500 and 600 K, then growing and converging to a linear dependence on T_O for large temperatures. The COP of CNTs is shown to remain about the same and approximately equal to 8. These results are shown to be weakly depend on CNT diameter and chirality but not on length. The isothermal entropy change of the CNTs due to the eC is also estimated and shown to depend nonlinearly on T_O values. These results predict that CNTs can be considered versatile nanoscale solid refrigerators able to efficiently work over a large temperature span.

DOI: 10.1103/PhysRevB.106.165413

I. INTRODUCTION

Concerns regarding the reduction of greenhouse gas emissions and the increasing demand for cooling have motivated intense research on the development of alternative methods to provide environment friendly cooling devices [1–12]. One of these alternatives is based on the caloric effect, i.e., the change of the temperature of an object when it is subjected to change of an external field [1,2]. The external field can be of electric, magnetic, or elastic/mechanical nature, or a combination of two or more of them. An important advantage of using the caloric effect to develop new cooling devices is that the refrigerant could be solid instead of vapor, which is beneficial for the reduction of greenhouse gases. An advantage for the vapor-compression process, however, is that its industry is so well developed that its refrigerators are not only reliable but also reach efficiencies as high as 60% of the Carnot one [3,12,13]. Solutions for the emission of greenhouse gases by vapor-compression refrigerators are also being thought of in terms of developing new environment friendly fluids or gases [10].

Nevertheless, another advantage of considering caloric effects of solid refrigerants is the possibility to scale down the system and/or applications [14,15]. Vapor-compression technologies cannot be scaled down [8,14,15]. In particular, amongst the caloric effects, the elastocaloric effect (eC) has been considered a promising efficient, nontoxic, and noise-free cooling method [15,16], with a predicted efficiency reaching values as large as 87% of Carnot efficiency [13]. eC is the caloric effect under the stimulus of applied strains to the material. Examples of known promising materials for the eC are Ni-Ti [7,13] and Cu-Zn-Al [16,17] shape memory alloys, $Ni_{57}Mn_{18}Ga_{21}In_4$ [18] and CoVGa [19] alloys, CaF_2 [20], and natural rubber [21,22].

In view of the advantages of the eC, some computational studies have been performed to predict the eC and the coefficient of performance (COP) of some structures at nanoscale. Lisenkov *et al.* [23] and Zhang [24] were the first to estimate the eC in carbon and boron-nitride (BN) nanotubes, respectively. They have found that the eC values of carbon (BN) nanotubes are up to 30 K (65 K) for 3% (9%) strain. Cantuario and Fonseca [25] were the first to estimate the COP of carbon nanotubes (CNTs) used as eC-based solid refrigerators. They simulated the refrigerator under Otto-like thermodynamic cycles operating at room temperature. The COP is defined as the ratio of the cooling to input power. Cantuario and Fonseca showed that CNTs present COP values between 4 and 6, which is comparable to the COP values of Ni-Ti and other shape memory alloys [7,17]. Other studies have shown the effects of adhesion on the eC of graphene [26], and the eC in ZnO nanowires [27]. Recent caloric studies on nanostructures are barocaloric [28,29] and electrocaloric effects [30].

*Corresponding author: afonseca@ifi.unicamp.br

Most of the above studies predict the eC at operating temperatures (T_Os) around 300 K. Few ones have studied the eC and its efficiency at certain T_O windows [16,31,32]. Sehitoglu *et al.* [31] and Chen *et al.* [32] predicted a maximum T_O window of eC in some Ni-Ti based shape memory alloys of about 100 K, while Mañosa *et al.* [16] have got a little bit wider temperature window of 130 K. These values are limited by the fact that the eC in these materials comes from phase transition changes. The eC in CNTs and BN nanotubes was shown not to depend on any phase transition [23,24]. Therefore, one might try to investigate the eC and its efficiency in these nanostructures at different values of T_O. In this work, the results for the eC and COP of CNTs as functions of T_O, from 300 to 2000 K, are presented. The choice of 2000 K as a superior limit in the present study comes first from the thermal stability of CNTs that is known to be about that value [33,34]. Second, it comes from the interest in the development of electronic devices capable to support high temperatures [35] or the need for the development of efficient refrigerators [36]. Examples of applications are in aircraft engines, hypersonic jets, exploration of hot planets, geothermal exploration, etc. [35]. Although these examples are for devices subject to at most 1100 K, we extended the present theoretical analysis up to the temperature limits supported by CNTs [33,34] as predictions of their cooling capacity at these extreme conditions for future developments. The dependence of these properties on CNT length and chirality is also investigated as CNTs are commonly synthesized at different lengths and the production of CNTs of chosen chirality remains a challenge [37]. We will see that the eC, represented by the change ΔT in temperature due to a maximum of 10% of applied strain, has a minimum at T_O values between 500 and 600 K, then grows towards a linear dependence on T_O, for large T_O, while maintaining roughly the same performance. The isothermal entropy change ΔS is also estimated and shown to grow, then converge to a certain value with increasing T_O. These results do not depend on CNT size, but weakly on the CNT chirality.

Section II presents the structure models, the theory behind the eC, and the computational methods to find ΔT, ΔS, and COP. Section III presents the results and discussion. Section IV summarizes the main results of this study.

II. STRUCTURE MODELS, EC THEORY, AND COMPUTATIONAL METHODS

Graphene is a planar hexagonal lattice of carbon atoms. CNTs are hexagonal lattices of carbon atoms drawn on a cylindrical surface. They can be imagined as being formed by rolling up pieces of graphene sheets around a certain axis. Different CNTs are represented by two integer parameters, n and m, that uniquely define its diameter and chiral angle. They are, then, called (n, m) CNTs and those where $m = n$ ($m = 0$) are called "armchair" ("zigzag") because of the shape of their edges. See, for example, Refs. [37,38] for more detailed geometrical descriptions of CNTs in terms of n and m. The following CNTs were considered in the present study: (6,6), (7,4), (8,8), (10,0), (9,7), and (14,0). Their atomic structures are shown in Fig. 1. (8,8) and (10,0) CNTs were chosen to compare the results with previous calculations [23,25]. The pairs of tubes (6,6) and (7,4) and (9,7) and (14,0) were chosen

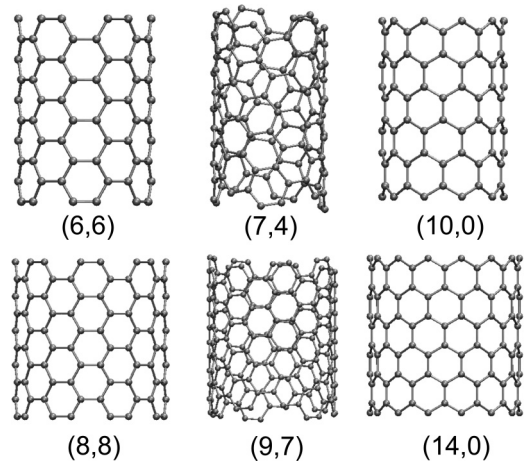

FIG. 1. Pieces of the atomic structures of (6,6), (7,4), (8,8), (10,0), (9,7), and (14,0) CNTs that were studied here. CNTs with chiral parameters like (n, n) and $(n, 0)$ are called "armchair" and "zigzag," respectively, because of the shape of their edges.

because their diameters are approximately equal to those of (8,8) and (10,0) CNTs, respectively ($d_{(6,6)} \approx d_{(7,4)} \approx d_{(10,0)} = 10\frac{a}{\pi}$, and $d_{(8,8)} \approx d_{(9,7)} \approx d_{(14,0)} = 14\frac{a}{\pi}$, with $a = a_{cc}\sqrt{3}$, and a_{cc} being the carbon-carbon bond distance). The test of the dependence of the eC on CNT chirality will be done for tubes having the same diameter and length. Two length sizes were analyzed: 10 and 50 nm.

In theory, the eC effect can be represented by two parameters, the isothermal change of the entropy, ΔS_{ISO}, and/or the adiabatic change of temperature, ΔT_{ADI}, of the material due to the variation of the strain ε. The entropy of an eC material can be written in terms of temperature T and the applied strain ε, so the following thermodynamic equation can be written [39]:

$$dS(T,\varepsilon) = \left(\frac{\partial S}{\partial \varepsilon}\right)_T d\varepsilon + \left(\frac{\partial S}{\partial T}\right)_\varepsilon dT. \tag{1}$$

Using the Maxwell relation $(\frac{\partial S}{\partial \varepsilon})_T = (\frac{\partial \sigma}{\partial T})_\varepsilon$, where σ is the applied stress on the eC material, and considering $dT = 0$ ($dS = 0$) for the isothermal (adiabatic) application of strain, ΔS_{ISO} and ΔT_{ADI} can, respectively, be obtained from appropriate integrations of Eq. (1):

$$\Delta S_{ISO} = \int_{\varepsilon_0}^{\varepsilon_F} \left(\frac{\partial \sigma}{\partial T}\right)_\varepsilon d\varepsilon, \tag{2}$$

$$\Delta T_{ADI} = -\int_{\varepsilon_0}^{\varepsilon_F} \frac{T}{C}\left(\frac{\partial \sigma}{\partial T}\right)_\varepsilon d\varepsilon, \tag{3}$$

where ε_0 and ε_F are initial and final strains during the corresponding thermodynamic process, and C is the heat capacity at constant strain ε, $C = (\frac{dQ}{dT})_\varepsilon = T(\frac{dS}{dT})_\varepsilon$.

Both ΔS_{ISO} and ΔT_{ADI} quantities are not trivial to measure or calculate, so we are going to characterize the eC effect in CNTs by "measuring" ΔT_{ADI} through computational numerical experiments and using it to estimate the corresponding ΔS_{ISO} (see, below, a derivation of an expression for ΔS_{ISO} in terms of ΔT_{ADI}). The CNTs eC and efficiency will be investigated considering an Otto-like thermodynamic cycle

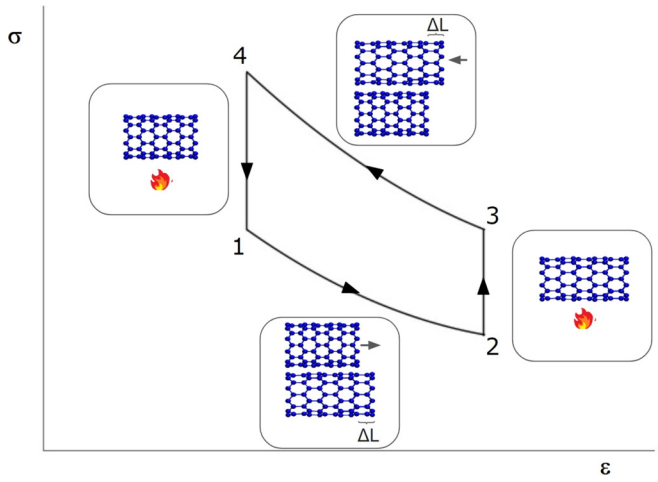

FIG. 2. Thermodynamic cycle formed by two processes of adiabatic expansion, $\{1 \to 2\}$ and $\{3 \to 4\}$, and two heat exchange processes, $\{2 \to 3\}$ and $\{4 \to 1\}$, with fixed volume in a thermal reservoir at a certain T_O. ΔL is the amount of tension strain applied to the nanotube during the adiabatic expansion.

consisting of $\{1 \to 2\}$, an adiabatic tensile strain process, departing from the CNT previously equilibrated at a given operating temperature T_O, followed by $\{2 \to 3\}$, an isostrain heat exchange process of the tensioned CNT with a thermal bath at T_O, then $\{3 \to 4\}$ application of another adiabatic, now tensile release, strain process, to bring back the CNT to the initial strain, and, to complete the cycle, the application of $\{4 \to 1\}$, another isostrain heat exchange process with a thermal bath at temperature T_O. Figure 2 illustrates the form of the Otto-like thermodynamics cycle in terms of the pressure-volume (pV) diagram, with the processes above numbered from 1 to 4 according to the above description. Otto cycles have been considered in previous eC studies [25,32].

ΔS_{ISO} is not trivial to calculate from Eq. (2). An isothermal process taking the system from strain ε_0 to strain ε_F at constant temperature T_O would be represented by a line joining the states 1 and 3 (or a $\{1 \to 3\}$ process) in Fig. 2. As the entropy is a thermodynamic state quantity, we can, in fact, choose another path to calculate ΔS_{ISO} between states 1 and 3. We can, for example, go from state 1 to state 3 by first following the $\{1 \to 2\}$ process, and then following the $\{2 \to 3\}$ process as shown in Fig. 2. Each one of these processes corresponds to a given change in entropy, $\Delta S_{\{1\to2\}}$ and $\Delta S_{\{2\to3\}}$, respectively, so ΔS_{ISO} can be obtained by summation of $\Delta S_{\{1\to2\}} + \Delta S_{\{2\to3\}}$. $\Delta S_{\{1\to2\}} = 0$ because the $\{1 \to 2\}$ process is adiabatic. The entropy change during the isostrain process $\{2 \to 3\}$ can be calculated as $\Delta S_{\{2\to3\}} = \int_2^3 dQ/T$. As $C = (\frac{dQ}{dT})_\varepsilon$, or $dQ = CdT$, we obtain

$$\Delta S_{ISO} = \Delta S_{\{2\to3\}} = \int_{T_F}^{T_O} \frac{C}{T} dT \cong C \ln\left(\frac{T_O}{T_F}\right), \tag{4}$$

where T_O is the operating temperature (initial in the process), T_F is the temperature at the final applied adiabatic strain ε_F, and the heat capacity was considered to be approximately constant in the temperature interval, $\Delta T_{ADI} = T_F - T_O$. Equation (4) can be further simplified to relate ΔS_{ISO} to ΔT_{ADI} by expanding it up to second order in $\Delta T_{ADI}/T_O$:

$$\Delta S_{ISO} \cong -C \left(\frac{\Delta T_{ADI}}{T_O}\right)\left(1 - \frac{\Delta T_{ADI}}{2T_O}\right). \tag{5}$$

The efficiency of the cycle is computed in terms of the COP, defined as

$$\text{COP} = \frac{Q_F}{W_C}, \tag{6}$$

where Q_F and W_C are the heat exchanged by the refrigerant and the region to be cooled, and the total work on one cycle, respectively. The first can be calculated by

$$Q_F = mC\Delta T_{ADI}, \tag{7}$$

where m and C are the mass and specific heat capacity of the CNT, and ΔT_{ADI} is the change in temperature due to the adiabatic application of tensile strain to the structure. Equation (3) will not be used to obtain ΔT_{ADI} because although the stress σ on the CNTs can be inferred from molecular dynamics (MD) simulations, its definition depends on the ill-defined cross-sectional area of the CNTs. As the temperature can be directly obtained from the simulations, ΔT_{ADI} will be obtained directly from those. From now on, we will omit the subscript "ADI" from "ΔT" as it will always correspond to the eC adiabatic change of temperature. However, we have to distinguish the real ΔT, herein called ΔT_{REAL}, from the ΔT obtained from the computational simulations, herein called ΔT_{MD}, because the classical MD simulations predict values of heat capacity that follows the Dulong-Petit law, while quantum mechanical effects are significant at certain values of temperature. In order to consider the real heat capacity, C_{REAL}, of the CNTs that obey the Debye theory, a relation between ΔT_{REAL} and ΔT_{MD} should be found. It is, in fact, simple and comes from the exchanged heat with the thermal bath during the isostrain process that is given by $Q_F = mC_{REAL}\Delta T_{REAL} = mC_{MD}\Delta T_{MD}$. So,

$$\Delta T_{REAL} = \left(\frac{C_{MD}}{C_{REAL}}\right)\Delta T_{MD}. \tag{8}$$

In order to obtain ΔT_{REAL}, we need to obtain the values of C_{REAL} for CNTs, for every temperature. Experimental values of C_{REAL} for CNTs are only available at temperatures smaller than or equal to 300 K [40]. As the Debye temperature of carbon structures is larger than 300 K [41], it is important to find out a way to estimate the C_{REAL} for CNTs at temperature values within the range 300–2000 K. It can be done using, for example, the theoretical approach developed by Mir *et al.* [42]. Based on the Debye's formula, the heat capacity of a solid can be written as [42,43]

$$C_{REAL}(T) = C^{TE}\left(\frac{T}{T_D}\right)^3 \int_0^{T_D/T} \frac{x^4 e^x}{(e^x - 1)^2} dx, \tag{9}$$

where T_D is the Debye temperature given by $T_D = h\nu_D/k_B$, with h and k_B being the Planck and Boltzmann constants, respectively, and ν_D the Debye frequency of the material that, for carbon nanotubes, is equal to 4.3867×10^{13} s^{-1} [42]. It gives $T_D \cong 2107$ K. The value of C^{TE} can be obtained using Eq. (9) with the known value of the $C_{REAL} = 645$ J kg^{-1} K^{-1} at $T = 300$ K as considered in previous studies [23,40]. We found $C^{TE} = 10\,216.4$ J kg^{-1} K^{-1}, that can be, then, used to

TABLE I. Values of the real heat capacity C_{REAL} of CNTs for different operating temperature values T_{O} considered in this work, calculated by Eq. (9) and the method described in the text.

T_{O} (K)	300	400	500	600	700	800
C_{REAL} (J kg^{-1} K^{-1})	645	1151.3	1607.0	1971.8	2252.2	2465.8
T_{O} (K)	900	1000	1100	1200	1300	1400
C_{REAL} (J kg^{-1} K^{-1})	2629.4	2756.1	2855.6	2934.7	2998.5	3050.5
T_{O} (K)	1500	1600	1700	1800	1900	2000
C_{REAL} (J kg^{-1} K^{-1})	3093.4	3129.2	3159.3	3184.8	3206.7	3225.5

calculate C_{REAL} for the values of operating temperatures in the range 400–2000 K. Table I shows the values of C_{REAL} obtained from the above method. Section S1 of the Supplemental Material (SM) [44] shows a graphic of $C_{\text{REAL}}(T)$ for $0 < T < 3000$ K, using Eq. (9) and the above value of C^{TE} in order to verify the Debye curve for CNTs. In our calculations for the real specific heat of all CNTs, C_{REAL}, we assumed that its value does not depend on the chiral parameters of the CNTs. In fact, as shown in Table II, MD simulations showed that C_{MD} are weakly dependent on the type of CNTs. Equation (8) assumes that C_{REAL} is roughly constant within the interval given by ΔT_{REAL}. An analysis estimating the error in the calculation of ΔT_{REAL} from this assumption is made in Sec. S2 of the SM [44], and shows that our results are good approximations for the expected values of the eC.

The total work on one thermodynamic cycle of the eC process, W_{C}, can be calculated as follows. As the adiabatic processes of the cycle are performed without heat exchange between the system and the exterior media, the total energy before, E_{B}, and after, E_{A}, the application of tension or tension-release to the CNT can be computed and the work done or received by the CNT can be simply calculated as

$$W_{\text{C}} = (E_{\text{A}} - E_{\text{B}})_{\text{TENSION}} + (E_{\text{A}} - E_{\text{B}})_{\text{TENSION-RELEASE}}. \tag{10}$$

No work is done or received by the CNT under the heat exchange processes $\{2 \rightarrow 3\}$ and $\{4 \rightarrow 1\}$, because its size is kept fixed during them. When tension is applied to the CNT, work from the external media is done on it, so its total energy increases, or $(E_{\text{A}} - E_{\text{B}})_{\text{TENSION}} > 0$. When allowing the tension to be released, the CNT energy decreases, or $(E_{\text{A}} - E_{\text{B}})_{\text{TENSION-RELEASE}} < 0$. The sum of these terms, then, represents the net work performed on the CNT during one thermodynamic cycle.

The protocols of MD simulations are given as follows. They were performed with the software LAMMPS (Large-scale Atomic/Molecular Massively Parallel Simulator) [45]. The adaptive intermolecular (AI) reactive empirical bond order (REBO) [46,47] classical force field was used to simulate the carbon-carbon interactions. AI + REBO is a well-known potential used to simulate structural, mechanical, and thermal properties of carbon nanostructures [48–57]. Besides, it has been used before to obtain the eC properties of CNTs and graphene [23,25,26].

TABLE II. Values of the MD heat capacity C_{MD} (J kg^{-1} K^{-1}) of CNTs from the MD simulations.

(6,6)	(7,4)	(8,8)	(10,0)	(9,7)	(14,0)
2065,07	1987,82	2051,51	2072,43	2056,94	2057,84

The structure of all CNTs studied here was first optimized through energy minimization algorithms and, then, equilibrated at T_{O} before starting the thermodynamic cycle previously described. The energy minimizations were performed imposing periodic boundary conditions (PBCs) along the CNT axis including the possibility to relax the size along the PBC direction. We followed a protocol of energy minimizations that ensures finding out the structure of smallest energy by performing combinations of energy minimization and free evolution algorithms as suggested by Sihn *et al.* [58] and recently implemented by Kanegae and Fonseca [59] in a study of graphynes. Thermal equilibration of the CNTs is performed by fixing the carbon atoms at the extremities and then applying a Langevin thermostat to all other atoms with damping factor of 100 fs and time step of 0.5 fs, for a total time of 60 ps. Although previously energy minimized, performing thermal equilibration on a CNT structure with fixed extremities might generate internal thermal stresses due to thermal expansion. However, the REBO potential predicts CNT axial linear thermal expansion coefficients of the order of $\sim 10^{-6}$ K^{-1} [45,60–62], from negative to positive values in a wide range of temperatures. So, in the temperature span of about 2000 K, the thermal strain will be maximum about $\sim 10^{-3}$, or $\sim 0,1\%$, that is much less than the 10% of maximum strain considered in this study. We will, then, neglect the thermal expansion effects.

The choice of the value of 10% as maximum tensile strain comes first from the fact that Cantuario and Fonseca [25] have chosen this value and their results can be compared to the ones obtained here. In addition, theoretical predictions indicate that CNTs can withstand up to 20% of tensile strain before breaking [63,64]. Recent experiments have shown that at large temperatures, they can be tensile strained up to 280% [65].

The adiabatic processes were simulated by keeping one end of the CNT fixed and applying a constant speed to the atoms of the other end. The atoms between the extremities have the initial velocities set to be compatible with a Boltzmann distribution corresponding to the thermal equilibrium at the operating temperature T_{O}. They are not thermostatted during the adiabatic processes. Fixing the speed of the moving carbon atoms at one end of the CNT and the total simulation time fixes the strain rate of the tensile or tensile-release processes. In order to obtain a better precision on the eC effect during the tensile strain simulations, the CNTs are strained using a time

step much smaller than that of usual simulations of carbon nanostructures using the AIREBO potential. The value of 0.02 fs of the time step (25 times smaller than the usual 0.5 fs of the time step) was used by a total amount of time of 32 ps (or 1 600 000 total simulation steps) to give 10%/32 ps or 0.003 125 ps^{-1} of strain rate, the same value used in previous studies [23,25]. As we shall see in the next section, the strain rate can affect the results for CNTs of different lengths. In order to keep the same strain rate and time step, the longer the CNT, the smaller the chosen speed of movement of the atoms of its nonfixed extremity and the longer the total simulation time. The reason is that the longer the CNT, the larger the time needed for the atoms far from those being pulled to feel the strain and equilibrate. In the heat exchange, the atoms of both ends of the CNT are kept fixed and the thermal equilibrium simulation of the remaining atoms are performed at T_O using a Langevin thermostat with damping factor of 100 fs and time step of 0.5 fs, for a total time of 60 ps.

The eC temperature variation ΔT_{MD} from the MD simulations will be computed as the difference between T_O and the last point of a moving average (over 1000 points) curve of temperature versus time collected along the adiabatic tensile simulations of the CNTs every 2 fs (or every 100 steps, which gives 16 000 data points). As explained above, the eC corresponding to the real temperature change ΔT_{REAL} is obtained using Eq. (8) and the values of C_{REAL} shown in Table I for each value of the operating temperature T_O. The MD values of the heat capacity, C_{MD}, are obtained from running previously series of MD simulations with each CNT, each simulation at a different value of temperature ranging 300–2000 K in steps of 50 K. From the slope of the energy versus temperature of each CNT obtained from these simulations, C_{MD} is determined. Each simulation is run by 60 ps with fixed extremities.

For the calculation of the COP, it is enough to use the value of ΔT_{MD} because $Q = mC_{MD}\Delta T_{MD}$. The work per cycle, W_C, is calculated by Eq. (10) where E_A and E_B are taken from the MD simulations.

III. RESULTS AND DISCUSSION

In this section, the results for the eC, ΔT and ΔS and the COP of all CNTs for a range of operating temperatures T_O from 300 to 2000 K are presented, including the dependence of these properties on the CNT size. The results for all CNTs of 10 nm length are presented first, including the analysis of the dependence on the CNT chirality and diameter. The length dependence of the eC and COP of CNTs is presented later.

Preliminary results of the C_{MD} of all CNTs are shown in Table II. The curves of energy versus equilibrium temperature of all CNTs from which the data shown in Table II were obtained are shown in Sec. S3 of the SM [44].

A. eC and COP of CNTs

Figure 2 shows the eC, ΔT_{REAL}, and ΔS (per kg) of all CNTs of 10 nm length studied here, subjected to the thermodynamic refrigerator cycle described in the previous section, running at operating temperatures ranging 300–2000 K. Quantum mechanical effects on the heat capacity of CNTs affect the dependence of ΔT_{REAL} on T_O. It presents a minimum in the considered operating temperature interval and after that, it grows towards a linear dependence on T_O when $T_O \to \infty$. As the heat capacity of a system tends to a constant according to the Dulong-Petit law, the linear growth of ΔT_{REAL} reflects this limit. Figure S4.1 in Sec. S4 of the SM [44] shows the linear dependence of the values of ΔT_{MD} on T_O. As the results for ΔT_{MD} reflect only the classical behavior of the heat capacity of CNTs, the linear growth of ΔT_{REAL} on T_O, for large T_O, represents the Dulong-Petit law when $T_O \to \infty$.

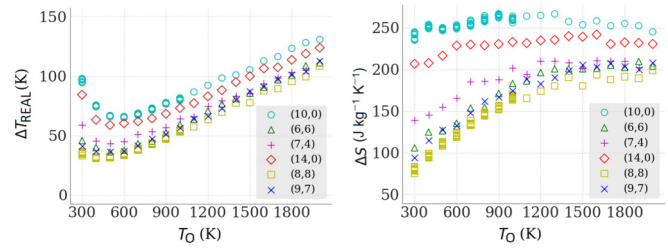

FIG. 3. Adiabatic temperature change ΔT_{REAL} (left panel) and the specific (per kg) isothermal change of entropy ΔS (right panel) versus operating temperature T_O of all CNTs studied here with 10 nm length. For (8,8) and (10,0) CNTs, results from the simulations of ten different microcanonical states corresponding to the same thermodynamic macroscopic states (same T_O, zero pressure, and size) are superposed.

In the seminal study by Cantuario and Fonseca [25], fluctuations of the eC and COP of CNTs have not been estimated. In the present work, for the (8,8) and (10,0) CNTs, they were calculated for a subrange of operating temperatures from 300 to 1000 K. Ten different microcanonical states corresponding to the same thermodynamic macroscopic states (same T_O, zero pressure, and size) were considered and subjected to the same thermodynamic cycle. Different microcanonical states can be computationally obtained by using different values of *seed* in the algorithms that generate the initial distribution of velocities corresponding to the T_O temperature, or simulate the thermal bath. The idea is to estimate the fluctuations in the eC and COP of the CNTs under the same values of T_O, in order to further verify if they depend on different T_Os. In Fig. 2, the superposed circle and squared points for each temperature in the interval from 300 to 1000 K correspond to the simulated eC of ten different microcanonical states of the (10,0) and (8,8) CNTs. We can clearly see that the deviations from the average values are relatively small for both the eC ΔT_{REAL} and ΔS. We then decided to extend these calculations for T_O up to 2000 K without repeating for different microcanonical states. Also, we decided to not repeat the simulations for different microcanonical states to obtain the eC of the other CNTs.

As Fig. 3 shows, ΔT_{REAL} of the zigzag CNTs are a few tens of Kelvin larger than that of other CNTs. Besides, the smaller the T_O, the larger this difference in ΔT_{REAL}. It might be a consequence of differences in the isothermal entropy changes among different nanotubes. The right panel of Fig. 3 presents the results for ΔS of all CNTs and it is possible to see that the isothermal entropy change in zigzag CNTs is larger than that

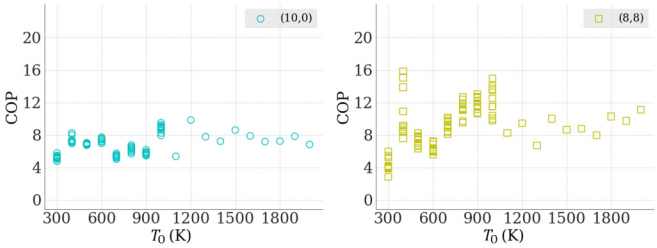

FIG. 4. COP of the (10,0) and (8,8) CNTs for each T_O for the full range 300–2000 K. For the subrange 300–1000 K, the results for the COP of the (10,0) and (8,8) CNTs corresponding to each of the ten different microcanonical states are shown.

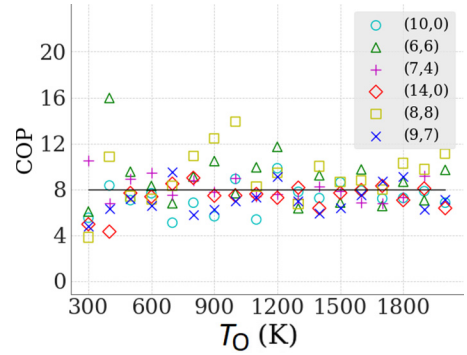

FIG. 5. COP of all CNTs of 10 nm length studied here for each T_O from 300 to 2000 K. For the (8,8) and (10,0) CNTs, the values of COP shown here at the subrange 300–1000 K were averaged over the simulations of ten different microcanonical states. The horizontal line represents the average of all values.

of the other CNTs. The entropy change is roughly constant for the zigzag CNTs while for the other CNTs, it increases with T_O and roughly converges after $T_O \sim 1000$ K. Another possible reason for the different eC results between zigzag and other types of CNTs comes from the geometry of these CNTs. As can be seen in Fig. 1, the zigzag CNTs possess more carbon-carbon bonds aligned with the direction of the applied tension strain than the armchair or other CNTs. As the eC comes from the thermal response of the material to the applied deformation, more carbon-carbon bonds participate in such response in zigzag CNTs. In armchair CNTs, for example, it is easy to see that some carbon-carbon bonds are orthogonal to the CNT axis and these bonds are certainly not strained due to the applied stress. Thinking about the carbon-carbon bond as being a local spring, it is like the zigzag tubes have more springs that feel and respond to the external applied stress more than the other tubes. The relation between strain in CNTs and entropy change will be investigated in more detail in the future.

Figure 3 also allows us to observe the weak dependence of the eC on the CNT diameter. When comparing the eC of CNTs of the same type of chirality, we notice that the larger the diameter, the smaller the values of ΔT_{REAL} and ΔS. Figure S4.2 in the SM [44] shows the values of ΔT_{MD} for each pair of tubes of the same chirality but different diameters.

Figure 4 shows the COP of the (10,0) and (8,8) CNTs for each T_O value in the full range 300–2000 K. Here, as in Fig. 3, for the subrange 300–1000 K, the results for the COP are shown for every simulation with a statistically different microcanonical state. Differently from the eC values, the COP of the CNTs visibly fluctuates with different microcanonical states, at least with large magnitude for the (8,8) CNT. However, the averages of these COP values at each T_O from 300 to 1000 K are not so different from those that were calculated at larger temperatures. This suggests that the COP of CNTs might not depend on the operating temperature of the refrigerator. In order to verify the generality of this result, we plotted together, and showed in Fig. 5, the COP of all CNTs studied here at the full T_O range.

Figure 5 allows us to conclude that although the COP of a refrigerator using the eC of the CNTs fluctuates significantly, it is not possible to identify any special dependence on the operating temperature T_O. This is, in fact, a good result because it indicates that CNTs can be valuable solid refrigerators with good efficiency running at a large temperature span. Most of the simulations resulted in COP > 4.

Cantuario and Fonseca [25] have calculated the values of the COP of (8,8) and (10,0) CNTs, 6.5 and 4.1, respectively. Although they have not performed statistically independent thermal simulations in order to obtain an estimate of fluctuations in the COP, their values are within the fluctuations found here and shown in Figs. 4 and 5.

In order to obtain the COP, it is necessary to calculate the work received by the CNT during one thermodynamical cycle, W_C. In Fig. S5 of the SM [44], we show two examples of how the total energy of two different CNTs varies with time during their adiabatic expansion and contraction, at two different T_O values.

B. Length dependence of the eC and COP of CNTs

The eC and COP of (10,0) and (8,8) CNTs of 50 nm length are presented in this subsection. The same thermodynamic cycle simulated with all 10-nm-length CNTs was applied to the 50-nm ones, but for temperature values only between 300 and 1000 K. The simulations were performed with the same parameters and conditions as previously, except for the total simulation times of the adiabatic processes that were changed in order to verify the effect of the strain rate on the results.

The first tests consisted of identifying the largest strain rate for which the eC results become independent on the rate.

Table III shows the values for ΔT, ΔS, and COP of 50-nm (10,0) CNTs obtained from simulations of the full thermodynamical cycle at $T_O = 300$ K, with the same parameters and conditions as in the previous section (i.e., 5 nm or 10% of total tensile strain and time step $= 0.02$ fs), but for different strain rates represented by the values of the time of the tensile strain and tensile-release strain simulations. While ΔT and ΔS did not change significantly, the COP increases with the total simulation times up to 128 ps. For times equal to or larger than 128 ps, the COP converges. This result might reflect the effect of the strain rate that becomes more relevant for long tubes and the same tensile strain simulation times considered for short tubes. The larger the strain rate, the lesser the time the

TABLE III. Values of the eC ΔT, ΔS, and COP of (10,0) CNT of 50-nm length, simulated at $T_O = 300$ K, for different values of the total time of the adiabatic tension and tension-release simulations. The time step and amount of strain of these simulations were all the same and equal to 0.02 fs and 10%, respectively, so the differences are in the strain rate.

Simulation time (ps)	Strain rate (nm ps^{-1})	ΔT_{MD} (K)	ΔT_{REAL} (K)	ΔS (J kg^{-1} K^{-1})	COP
32	0.15625	28.39	91.22	225.81	1.89
64	0.078125	29.37	94.37	234.67	3.60
96	0.0520833	31.36	100.76	252.87	4.60
128	0.0390625	31.59	101.50	254.99	5.71
160	0.03125	31.57	101.44	254.82	6.87
200	0.025	29.76	95.62	238.22	5.72
250	0.02	30.17	96.94	241.95	6.09
320	0.015625	31.97	102.72	258.51	6.72

system has to equilibrate. For a 10-nm-length CNT, the total strain of 10% (or $\Delta L = 1$ nm) was simulated in 32 ps, which corresponds to a tensile strain speed of 0.031 25 nm/ps, or a strain rate of $10/32 = 0.3125\%$ ps^{-1}. For the strain rate on a 50-nm-length CNT to be the same as that of simulating 10% strain of a 10-nm-length CNT, the total simulation time should be increased proportionally. As 10% of 50 nm is 5 nm, we must ensure tensile strain of the structure during 5 nm /1nm times 32 or 160 ps (5 nm/160 ps = 1 nm/32 ps = 0.03125 nm/ps). As seen in Table III, from 128 ps of total simulation time, the COP reaches a value that roughly converges. Therefore, the value of $5/128 = 0.039\,062\,5$ nm/ps might be considered an estimate for the largest strain rate able to allow the CNT structure to equilibrate during the eC. Here, we decided to set the value of strain rate of the simulations of 50 nm CNTs to that used in the simulations of 10-nm-long CNTs (strain rate of 0.3125% ps^{-1}). It means that the total simulation time of the tensile strain and tensile strain release processes, to obtain the eC of the 50-nm-length CNTs at other values of T_O, is set to 160 ps.

Tables IV and V show the COP and ΔT_{REAL} of 10- and 50-nm-length (8,8) and (10,0) CNTs, for T_O ranging 300–1000 K. We note that the COPs for the longer CNTs, in average, remained the same as that of 10-nm-length CNTs. The values of ΔT_{REAL} are about the same too, i.e., there is no sign of length dependence of the eC in CNTs.

IV. CONCLUSIONS

The eC of CNTs of different lengths, chiralities, and diameters were obtained from MD simulations for a large temperature span. We show that while the COP of the CNTs as a solid refrigerant remains roughly the same for the range $300\ \text{K} \leqslant T_O \leqslant 2000$ K considered here, the eC ΔT and ΔS change nonlinearly with T_O. Classical thermal behavior is observed to occur for $T_O > 1000$ K since the dependence of ΔT on T_O becomes linear. The results show a weak dependence of the eC on CNT diameter and no dependence on length. The adiabatic temperature change ΔT and the isothermal entropy change ΔS of zigzag CNTs during one cycle of the simulated thermodynamic cycle of the refrigerator machine were shown to be larger than that of other chiral CNTs, mostly at low T_O.

Different from other good eC materials, the eC in CNTs does not depend on phase transitions. Therefore, CNTs can be explored as solid refrigerators at large ranges of operating temperatures. In particular, our results predict that not only is the eC significant at a large temperature span but also with approximately the same good efficiency with COP values estimated to be about 8. In view of the quest for new, safe, and low-cost refrigeration methods, together with the increasing miniaturization trends in technology, we believe the results from the present study will guide and motivate further experiments on the development of nanorefrigerators.

ACKNOWLEDGMENTS

T.N.Y.S. and A.F.F. acknowledge support from São Paulo Research Foundation (FAPESP) through Grants No. 2020/05333-1 and No. 2020/02044-9, respectively. A.F.F. is a fellow of CNPq–Brazil (303284/2021-8). We also acknowledge support from the John David Rogers Computing Center (CCJDR) at the Institute of Physics "Gleb Wataghin," University of Campinas.

TABLE IV. Values of the COP of (10,0) and (8,8) CNTs of 10- and 50-nm lengths for each T_O from 300 to 1000 K, for comparison.

CNT	L (nm)	300 K	400 K	500 K	600 K	700 K	800 K	900 K	1000 K	Average
(8,8)	10	4.35	10.70	7.34	6.43	9.22	11.25	11.88	12.18	9.17
	50	8.07	9.52	9.20	9.15	8.29	10.29	8.66	8.07	8.91
(10,0)	10	5.20	7.38	6.90	7.33	5.36	6.24	5.75	8.82	6.62
	50	6.87	5.73	6.65	6.74	5.61	5.90	4.45	5.41	5.92

TABLE V. Values of ΔT_{REAL} (K) of (10,0) and (8,8) CNTs of 10- and 50-nm lengths for each T_O from 300 to 1000 K, for comparison.

CNT	L (nm)	300 K	400 K	500 K	600 K	700 K	800 K	900 K	1000 K
(8,8)	10	35.12	31.26	32.00	34.12	38.19	43.04	47.72	54.08
	50	37.47	34.25	34.32	36.72	41.27	44.74	50.21	55.10
(10,0)	10	96.30	74.82	66.38	65.48	67.94	72.05	77.13	80.53
	50	101.44	74.74	70.70	69.36	70.03	73.12	73.06	80.50

[1] L. Mañosa, A. Planes, and M. Acet, Advanced materials for solid-state refrigeration, J. Mater. Chem. A **1**, 4925 (2013).

[2] X. Moya, S. Kar-Narayan, and N. D. Mathur, Caloric materials near ferroic phase transitions, Nat. Mater. **13**, 439 (2014).

[3] A. Chauhan, S. Patel, R. Vaish, and C. R. Bowen, A review and analysis of the elasto-caloric effect for solid-state refrigeration devices: Challenges and opportunities, MRS Energy Sustainability **2**, E16 (2015).

[4] M. Schmidt, A. Schütze, and S. Seelecke, Elastocaloric cooling processes: The influence of material strain and strain rate on efficiency and temperature span, APL Mater. **4**, 064107 (2016).

[5] J. Tušek, K. Engelbrecht, D. Eriksen, S. Dall'Olio, J. Tušek, and N. Pryds, a regenerative elastocaloric heat pump, Nat. Energy **1**, 16134 (2016).

[6] L. Mañosa and A. Planes, Materials with giant mechanocaloric Effects: Cooling by strength, Adv. Mater. **29**, 1603607 (2017).

[7] J. Frenzel, G. Eggeler, E. Quandt, S. Seelecke, and M. Kohl, High-performance elastocaloric materials for the engineering of bulk- and micro-cooling devices, MRS Bull. **43**, 280 (2018).

[8] C. Cazorla, Novel mechanocaloric materials for solid-state cooling applications, Appl. Phys. Rev. **6**, 041316 (2019).

[9] L. Mañosa and A. Planes, Solid-state cooling by stress: A perspective, Appl. Phys. Lett. **116**, 050501 (2020).

[10] M. O. McLinden, C. J. Seeton, and A. Pearson, New refrigerants and system configurations for vapor-compression refrigeration, Science **370**, 791 (2020).

[11] X. Moya and N. D. Mathur, Caloric materials for cooling and heating, Science **370**, 797 (2020).

[12] Y. Dong, M. Coleman, and S. A. Miller, Greenhouse gas emissions from air conditioning and refrigeration service expansion in developing countries, Annu. Rev. Environ. Resour. **46**, 59 (2021).

[13] J. Cui, Y. Wu, J. Muehlbauer, Y. Hwang, R. Radermacher, S. Fackler, M. Wuttig, and I. Takeuchi, Demonstration of high efficiency elastocaloric cooling with large ΔT using niti wires, Appl. Phys. Lett. **101**, 073904 (2012).

[14] F. Bruederlin, L. Bumke, C. Chluba, H. Ossmer, E. Quandt, and M. Kohl, Elastocaloric cooling on the miniature scale: A review on materials and device engineering, Energy Technol. **6**, 1588 (2018).

[15] M. Imran and X. Zhang, Reduced dimensions elastocaloric materials: A route towards miniaturized refrigeration, Mater. Design **206**, 109784 (2021).

[16] L. Mañosa, S. Jarque-Farnos, E. Vives, and A. Planes, Large temperature span and giant refrigerant capacity in elastocaloric Cu-Zn-Al shape memory alloys, Appl. Phys. Lett. **103**, 211904 (2013).

[17] S. Qian, Y. Geng, Y. Wang, J. Ling, Y. Hwang, R. Radermacher, I. Takeuchi, and J. Cui, a review of elastocaloric cooling: Materials, cycles and system integrations, Int. J. Refrig. **64**, 1 (2016).

[18] J. Wang, Q. Yu, K. Xu, C. Zhang, Y. Wu, and C. Jiang, Large room-temperature elastocaloric effect of Ni57Mn18Ga21In4 alloy undergoing a magnetostructural coupling transition, Scr. Mater. **130**, 148 (2017).

[19] Y. Niu, H. Chen, X. Zhang, S. Li, D. Cong, T. Ma, S. Li, J. Lin, and Y. -D. Wang, Achieving excellent superelasticity and extraordinary elastocaloric effect in a directionally solidified Co-V-Ga alloy, Scr. Mater. **204**, 114123 (2021).

[20] C. Cazorla and D. Errandonea, Giant mechanocaloric effects in fluorite-structured superionic materials, Nano Lett. **16**, 3124 (2016).

[21] Z. Xie, G. Sebald, and D. Guyomar, Temperature dependence of the elastocaloric effect in natural rubber, Phys. Lett. A **381**, 2112 (2017).

[22] C. M. Miliante, A. M. Christmann, E. O. Usuda, W. Imamura, L. S. Paixão, A. M. G. Carvalho, and A. R. Muniz, Unveiling the origin of the giant barocaloric effect in natural rubber, Macromolecules **53**, 2606 (2020).

[23] S. Lisenkov, R. Herchig, S. Patel, R. Vaish, J. Cuozzo, and I. Ponomareva, Elastocaloric effect in carbon nanotubes and graphene, Nano Lett. **16**, 7008 (2016).

[24] J. Zhang, Elastocaloric effect on the piezoelectric potential of boron nitride nanotubes, J. Phys. D: Appl. Phys. **50**, 415308 (2017).

[25] T. E. Cantuario and A. F. Fonseca, High performance of carbon nanotube refrigerators, Ann. Phys. (Berlin) **531**, 1800502 (2019).

[26] M. Li, Z. Guo, and T. Chang, Adhesion and stress-enhanced elastocaloric effect in graphene, Sci. China Technol. Sci. **63**, 297 (2020).

[27] S. Patel and M. Kumar, Elastocaloric effect in zinc oxide nanowire, Funct. Mater. Lett. **14**, 2150021 (2021).

[28] N. Ma and M. S. Reis, Anomalous acoustic phonons as the physical mechanism behind the adiabatic barocaloric effect on graphene, Sci. Rep. **9**, 219 (2019).

[29] J. Li, D. Dunstan, X. Lou, A. Planes, L. Mañosa, M. Barrio, J. -L. Tamarit, and P. Lloveras, Reversible barocaloric effects over a large temperature span in fullerite C60, J. Mater. Chem. A **8**, 20354 (2020).

[30] J. Zhang, Electrocaloric effects in monolayer germanium sulfide: A study by molecular dynamics simulations and thermodynamic analyses, J. Appl. Phys. **127**, 175105 (2020).

[31] H. Sehitoglu, Y. Wu, and E. Ertekin, Elastocaloric effects in the extreme, Scr. Mater. **148**, 122 (2018).

[32] H. Chen, F. Xiao, X. Liang, Z. Li, Z. Li, X. Jin, and T. Fukuda, Giant elastocaloric effect with wide temperature window in an Al-doped nanocrystalline Ti-Ni-Cu shape memory alloy, Acta Mater. **177**, 169 (2019).

[33] K. Méténier, S. Bonnamy, F. Béguin, C. Journet, P. Bernier, M. Lamy de La Chapelle, O. Chauvet, and S. Lefrant,

Coalescence of single-walled carbon nanotubes and formation of multi-walled carbon nanotubes under high-temperature treatments, Carbon **40**, 1765 (2002).

[34] Y. A. Kim, H. Muramatsu, T. Hayashi, M. Endo, M. Terrones, and M. S. Dresselhaus, Thermal stability and structural changes of double-walled carbon nanotubes by heat treatment, Chem. Phys. Lett. **398**, 87 (2004).

[35] M. Alhendi, F. Alshatnawi, E. M. Abbara, R. Sivasubramony, G. Khinda, A. I. Umar, P. Borgesen, M. D. Poliks D. Shaddock, C. Hoel, N. Stoffel, and T.-K. H. Lam, Printed electronics for extreme high temperature environments, Additive Manufacturing **54**, 102709 (2022).

[36] M. Wei, W. Cai, M. Xu, and S. Deng, Active cooling system for downhole electronics in high-temperature environments, J. Thermal Sci. Eng. Appl. **14**, 081009 (2022).

[37] F. Yang, M. Wang, D. Zhang, J. Yang, M. Zheng, and Y. Li, Chirality pure carbon nanotubes: Growth, sorting, and characterization, Chem. Rev. **120**, 2693 (2020).

[38] L. C. Venema, V. Meunier, Ph. Lambin, and C. Dekker, Atomic structure of carbon nanotubes from scanning tunneling microscopy, Phys. Rev. B **61**, 2991 (2000).

[39] D. J. Silva, J. Ventura, and J. P. Araújo, Caloric devices: A review on numerical modeling and optimization strategies, Int. J. Energy Res. **45**, 18498 (2021).

[40] J. Hone, B. Batlogg, Z. Benes, A. T. Johnson, and J. E. Fischer, Quantized phonon spectrum of single-wall carbon nanotubes, Science **289**, 1730 (2000).

[41] T. Tohei, A. Kuwabara, F. Oba, and I. Tanaka, Debye temperature and stiffness of carbon and boron nitride polymorphs from first principles calculations, Phys. Rev. B **73**, 064304 (2006).

[42] M. Mir, E. Ebrahimnia-Bajestan, H. Niazmand, and M. Mir, A novel approach for determining thermal properties of single-walled carbon nanotubes, Comput. Mater. Sci. **63**, 52 (2012).

[43] R. Eisberg and R. Resnick, *Quantum Physics of Atoms, Molecules, Solids, Nuclei, and Particles*, 2nd ed. (Hamilton, New York, 1985).

[44] See Supplemental Material at http://link.aps.org/supplemental/10.1103/PhysRevB.106.165413 for the details regarding the elastocaloric theory and data from the MD simulations.

[45] A. P. Thompson, H. M. Aktulga, R. Berger, D. S. Bolintineanu, W. M. Brown, P. S. Crozier, P. J. in't Veld, A. Kohlmeyer, S. G. Moore, T. D. Nguyen, R. Shan, M. J. Stevens, J. Tranchida, C. Trott, and S. J. Plimpton, LAMMPS - a flexible simulation tool for particle-based materials modeling at the atomic, meso, and continuum scales, Comput. Phys. Commun. **271**, 108171 (2022).

[46] D. W. Brenner, O. A. Shenderova, J. A. Harrison, S. J. Stuart, B. Ni, and S. B. Sinnott, a second-generation reactive empirical bond order (REBO) potential energy expression for hydrocarbons, J. Phys.: Condens. Matter **14**, 783 (2002).

[47] S. J. Stuart, A. B. Tutein, and J. A. Harrison, a reactive potential for hydrocarbons with intermolecular interactions, J. Chem. Phys. **112**, 6472 (2000).

[48] A. F. Fonseca, T. Borders, R. H. Baughman, and K. Cho, Load transfer between cross-linked walls of a carbon nanotube, Phys. Rev. B **81**, 045429 (2010).

[49] R. Grantab, V. B. Shenoy, and R. S. Ruoff, Anomalous strength characteristics of tilt grain boundaries in graphene, Science **330**, 946 (2010).

[50] M. Neek-Amal and F. M. Peeters, Lattice thermal properties of graphane: Thermal contraction, roughness, and heat capacity, Phys. Rev. B **83**, 235437 (2011).

[51] W. Gao and R. Huang, Thermomechanics of monolayer graphene: Rippling, thermal expansion and elasticity, J. Mech. Phys. Solids **66**, 42 (2014).

[52] N. C. B. Mostério and A. F. Fonseca, Thermal expansion behavior of holes in graphene nanomeshes, Phys. Rev. B **89**, 195437 (2014).

[53] A. R. Muniz and A. F. Fonseca, Carbon-Based nanostructures derived from bilayer graphene with zero thermal expansion behavior, J. Phys. Chem. C **119**, 17458 (2015).

[54] M. Chen, A. R. Muniz, and D. Maroudas, Formation and mechanical behavior of nanocomposite superstructures from interlayer bonding in twisted bilayer graphene, ACS Appl. Mater. Interfaces **10**, 28898 (2018).

[55] A. F. Fonseca and D. S. Galvão, Self-tearing and self-peeling of folded graphene nanoribbons, Carbon **143**, 230 (2019).

[56] G. Dhaliwal, P. B. Nair, and C. V. Singh, Uncertainty analysis and estimation of robust AIREBO parameters for graphene, Carbon **142**, 300 (2019).

[57] A. F. Fonseca, Twisting or untwisting graphene twisted nanoribbons without rotation, Phys. Rev. B **104**, 045401 (2021).

[58] S. Sihn, V. Varshney, A. K. Roy, and B. L. Farmer, Modeling for predicting strength of carbon nanostructures, Carbon **95**, 181 (2015).

[59] G. B. Kanegae and A. F. Fonseca, Effective acetylene length dependence of the elastic properties of different kinds of graphynes, Carbon Trends **7**, 100152 (2022).

[60] P. K. Schelling and P. Keblinski, Thermal expansion of carbon structures, Phys. Rev. B **68**, 035425 (2003).

[61] H. Jiang, B. Liu, Y. Huang, and K. C. Hwang, Thermal expansion of single wall carbon nanotubes, J. Eng. Mater. Technol. **126**, 265 (2004).

[62] C. Li and T.-W. Chou, Axial and radial thermal expansions of single-walled carbon nanotubes, Phys. Rev. B **71**, 235414 (2005).

[63] M. B. Nardelli, B. I. Yakobson, and J. Bernholc, Mechanism of strain release in carbon nanotubes, Phys. Rev. B **57**, R4277 (1998).

[64] Q. Zhao, M. Buongiorno Nardelli, and J. Bernholc, Ultimate strength of carbon nanotubes: A theoretical study, Phys. Rev. B **65**, 144105 (2002).

[65] J. Y. Huang, S. Chen, Z. Q. Wang, K. Kempa, Y. M. Wang, S. H. Jo, G. Chen, M. S. Dresselhaus, and Z. F. Ren, Superplastic carbon nanotubes, Nature (London) **439**, 281 (2006).